J. Chem. Thermodynamics 74 (2014) 169–183

Contents lists available at ScienceDirect

J. Chem. Thermodynamics

journal homepage: www.elsevier.com/locate/jct

Thermodynamics of confined nano-phases ☆

Keith E. Gubbins [a,*], Yun Long [b], Małgorzata Śliwinska-Bartkowiak [c]

[a] Department of Chemical & Biomolecular Engineering, North Carolina State University, Raleigh, NC 27695-7905, USA
[b] Department of Chemical & Biomolecular Engineering, National University of Singapore, 4 Engineering Drive 4, Singapore 117576, Singapore
[c] Institute of Physics, Adam Mickiewicz University, Umultowska 85, 61-614 Poznan, Poland

ARTICLE INFO

Article history:
Received 24 January 2014
Accepted 28 January 2014
Available online 7 February 2014

Keywords:
Confinement effects
Adsorption
Phase change
Wetting
Pressure tensor

ABSTRACT

We consider a phase of nano-scale dimensions (the adsorbate) confined within a porous material, and in thermal, chemical and mechanical equilibrium with a bulk phase of fixed temperature, pressure and composition. From a corresponding states analysis of the partition function for pores of simple geometry (*e.g.*, slit- or cylinder-shaped) we show that the principal system variables for most cases are the pore shape and width (expressed in terms of molecular diameters), H^*, and a microscopic wetting parameter, α_w, that is a measure of the relative strength of the adsorbate-wall and adsorbate–adsorbate interactions. We illustrate the utility of this model by considering experimental, theoretical and molecular simulation results for adsorption, (vapor + liquid) condensation for pure fluids and mixtures, freezing, and pressures for these confined nano-phases. The wetting parameter is shown to be of central importance, determining both the magnitude of the effects of confinement and also the qualitative behavior, for example, whether the freezing temperature is raised or lowered upon confinement. These confinement effects become larger as the pore width is reduced; reducing the pore width can also result in qualitative changes, such as phase changes. For pores of slit- or cylinder-shape there are two independent pressures within the pores, one acting normal to the pore walls and one (the tangential pressure) acting parallel to the walls. Molecular simulation results show that these two pressures, which are of the order thousands or tens of thousands of bars for small pores in equilibrium with a bulk phase at ambient pressure, differ greatly in magnitude and in their response to changes in the system and state variables.

1. Introduction

Fluid or solid phases of nano-scale dimensions, when in contact with a solid surface or confined within a narrow pore, such as occurs in a nano-porous solid (*e.g.*, carbons and oxides of various kinds), within a living cell, reverse micelle, or clathrate hydrate, have thermodynamic properties that are often very different from those of the macroscopic bulk material. These confinement effects arise because of reduced dimensionality and strong interaction of the molecules in the nano-phase with the confining walls. Examples of such effects are shifts in phase boundaries, the presence of new surface-driven phases, heats of adsorption, enhanced pressures, selective adsorption in the case of mixtures, and shifts in chemical equilibrium for reactions. In addition to these effects on thermodynamic properties, some familiar thermodynamic laws and concepts can break down at the nano-scale. These include Gibbs surface thermodynamics, including the concept of surface tension (for sufficiently small nano-phases there is no well-defined surface separating two bulk phases) and laws based on these concepts that include Kelvin, Laplace, Young, Gibbs–Thomson and similar equations. Similarly, the Second Law of Thermodynamics breaks down at the nano-scale, due to the increasingly large fluctuations that occur as system size is decreased. As noted by Maxwell in his review of Tait's book on thermodynamics [1]:

☆ Based on the 19th ROSSINI LECTURE presented at the 22nd International Conference on Chemical Thermodynamics, Buzios, Brazil, 06 August 2012. Previous Rossini lectures can be found in this Journal: first by Frederick D. Rossini himself in 1976, 8, 803–834; the second by Henry A. Skinner in 1978, 10, 309–320; the fourth by Edgar F. Westrum, Jr. in 1983, 15, 305–325; the fifth by Maxwell L. McGlashen in 1985, 17, 301–319; the sixth by E. Ulrich Franck in 1987, 19, 225–242; the seventh by Kenneth S. Pitzer in 1989, 21, 1–17; the eighth by Gerhard M. Schneider in 1991, 23, 301–326; the ninth by John S. Rowlinson in 1993, 25, 449–461; the 10th by Hendrick C. Van Ness in 1995, 27, 113–134; the 11th by Robert A. Alberty in 1997, 29, 501–516; the 12th by Stanley L. Sandler in 1999, 31, 3–25; the 13th by William A. Wakeham in 2001, 33, 1623–1642; the 14th by John M. Prausnitz in 2003, 35, 21–39; the 15th by Jean-Pierre Grolier in 2005, 37, 1226–1238; the 16th by Alexandra Novrotsky in 2007, 29, 2–7; the 17th by Jürgen Gmehling in 2009, 41, 731–747; the 18th by Gerd Mauer in 2011, 43, 143–160. Stig A. Sunner, appointed as the third Rossini Lecturer, would have given his lecture at Meresburg in August 1980 had he not died on 3 June 1980 (see this Journal, 1980, 12(8), i–ii).

* Corresponding author. Tel.: +1 919 513 2262; fax: +1 919 515 3465.
E-mail address: keg@ncsu.edu (K.E. Gubbins).

http://dx.doi.org/10.1016/j.jct.2014.01.024
0021-9614/

Hence the Second Law of Thermodynamics is continually being violated and that to a considerable extent in any sufficiently small group of molecules belonging to any real body.

In such nano-scale systems the Second Law is replaced by a fluctuation theorem that applies to small systems for short periods of time [2,3]. The fluctuation theorem leads to the Second Law in the thermodynamic limit ($N \to \infty$, $\rho = N/V$ = constant, where N and V are the number of molecules and volume).

A further complication in nano-scale systems is that some familiar properties may not be uniquely defined. Examples are the volume and the pressure. In the case of a confined nano-phase, we must make a choice of where to draw the system boundaries. For example, we might define the boundary as the surface drawn through the centers of the atoms on the wall's surface (a suitable choice for neutron scattering studies) or a surface that excludes some dead volume near the walls (often used in adsorption studies). For properties such as volume and pressure, we must make an operational definition [4].

Theory, including molecular simulation, and experiment have different strengths and limitations, and are to a large extent complementary in this area. Significant difficulties in experimental studies of confined nano-phases include measurement of the composition and structure of the confined phase, long-lived metastable states, preferential adsorption of trace components, and measurement of many properties of the confined phase, *e.g.*, pressures. Difficulties in theoretical and simulation studies include uncertainty about the detailed atomic structure of the confining medium (*e.g.*, pore morphology and topology in the case of porous materials), and about the force fields involved. Moreover, for large and flexible molecules or particles, such as polymers, proteins and colloids, insufficient computer power remains a limitation. This latter difficulty should be ameliorated in the next few years, when Exo-flop and faster supercomputers become available.

In this paper, we give an overview of the current state of knowledge of some of the main confinement effects on the thermodynamic behavior of nano-phases. In Section 2, we consider the conditions of equilibrium for the confined phase, and the principal variables that influence confinement effects. In Section 3, we discuss two examples of such effects: the effect of confinement on phase changes within the pores, and on the in-pore pressures.

2. Thermodynamics of confined phases

2.1. Condition of phase equilibrium

We consider a porous material (or other confining medium) that reaches equilibrium with a bulk phase, usually a gas or liquid, as shown schematically in figure 1. At equilibrium, the conditions are:

$$\begin{aligned} \mu_{\text{bulk}} &= \mu_{\text{confined}}, \\ T_{\text{bulk}} &= T_{\text{confined}}, \\ \nabla \cdot \mathbf{P} &= -\rho(\mathbf{r}) \nabla v(\mathbf{r}), \end{aligned} \tag{1}$$

where μ is chemical potential, T is temperature, $\mathbf{P}$ is the pressure tensor, and $\rho(\mathbf{r})$ and $v(\mathbf{r})$ are the number density and the external field acting at point $\mathbf{r}$. Subscripts *bulk* and *confined* indicate values for the bulk and pore phases, respectively.

The first two of these equations are the familiar conditions of thermodynamic equilibrium for bulk phases. We note that although the density and pressure vary rapidly with the position within the pore, the chemical potential is everywhere constant. The third equation is the condition of mechanical, or hydrodynamic equilibrium, and is the generalization to inhomogeneous

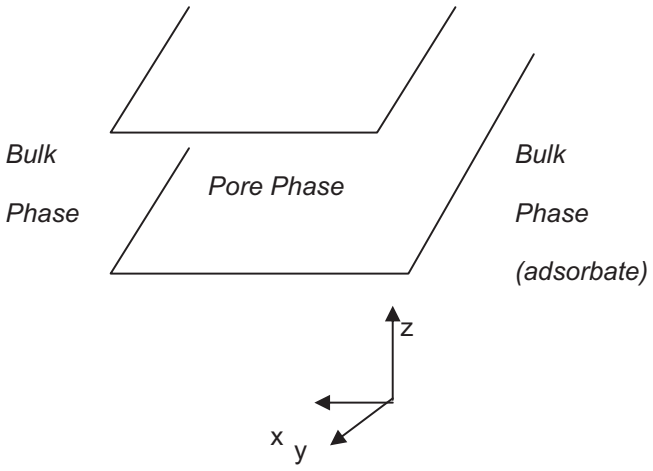

FIGURE 1. Equilibrium between a bulk phase and the pore phase.

phases of the usual hydrodynamic condition for bulk homogeneous phases. It arises from the requirement that there be no net momentum flow between the two phases at equilibrium (see reference [4], Section 8.3). In the applications considered here, there is no external field and so the hydrodynamic equilibrium condition becomes:

$$\nabla \cdot \mathbf{P} = 0. \tag{2}$$

The pressure within the pore is a second-order tensor; thus $P_{\alpha\beta}$ is the force per unit area in the β-direction acting on an element of surface pointing in the α-direction.

2.2. The principal independent variables; corresponding states analysis

For confined nano-phases, the number of system variables considerably exceeds those of temperature, pressure, and composition for bulk phases. These additional variables include the composition and structure of the adsorbent material, the size and shape of the pores, their morphology and topology, wall roughness, *etc.* In view of this added complexity, it is instructive to consider first a simple system in which the pores are of simple geometry with smooth walls, while the adsorbate molecules can be treated as effectively spherical as far as their intermolecular interactions are concerned. We consider an adsorbate (a) that is a pure substance confined in a slit-shaped pore of width H. There are two kinds of intermolecular potential energies involved, adsorbate–adsorbate, $u_{aa}(r)$, and adsorbate-solid (s), $u_{as}(r)$. For the interaction of a single adsorbate molecule with the solid surface, the structureless 10-4-3 potential of Steele [5,6] is often a good approximation,

$$u_{as}(z) = 2\pi\rho_s\sigma_{as}^2\varepsilon_{as}\Delta\left[\frac{2}{5}\left(\frac{\sigma_{as}}{z}\right)^{10} - \left(\frac{\sigma_{as}}{z}\right)^{4} - \left(\frac{\sigma_{as}^4}{3\Delta(z+0.61\Delta)^3}\right)^{3}\right]. \tag{3}$$

This expression is arrived at by integrating the pair interactions between an adsorbate molecule located at distance z from the pore wall over the positions of the atoms in the solid with which it interacts, and assuming that the solid atoms are arranged in layers separated by distance Δ, as in graphite. In this expression, ρ_s is the number of solid atoms per unit volume, and σ_{as} and ε_{as} are the usual parameters of size and energy well depth in the intermolecular pair potential energy, here taken to be the Lennard–Jones (12,6) model. Thus the 10-4-3 model treats the wall as structureless. This model ignores corrugations in the surface and is generally

a good approximation provided that the adsorbate molecules are reasonably large compared to the spacing of the wall atoms, and the temperature is not too low. For graphite surfaces, for example, where the spacing of the carbon atoms is about 0.14 nm, and for methane ($\sigma_{aa} \approx 0.37$ nm) as the adsorbate, the use of the 10-4-3 model gives results that are indistinguishable from those for a fully atomistic structured wall for temperatures down to about 80 K [7,8]. Equation (3) gives the interaction energy of an adsorbate molecule with one wall. The total potential energy due to both walls is

$$u_{a,pore}(z) = u_{as}(z) + u_{as}(H - z). \tag{4}$$

The important dimensionless variables for such a simple porous system can be identified by a corresponding states analysis. Since the chemical potential is everywhere constant it is convenient to use the grand canonical ensemble. The equilibrium condition requires that the grand free energy, $\Omega = A - \sum_i \mu_i \langle N_i \rangle = -PV$, where A is the Helmholtz energy and $\langle N_i \rangle$ is the average number of molecules of component i, be a minimum. The latter is given by:

$$\Omega = -kT \ln \Xi, \tag{5}$$

where Ξ is the grand partition function, and is given, in the usual semi-classical approximation, as

$$\Xi = \sum_{N \geqslant 0} \frac{e^{N\mu/kT}}{\Lambda^{3N} N!} \int_0^V \cdots \int_0^V d\mathbf{r}_1 d\mathbf{r}_2 d\mathbf{r}_3 \ldots, d\mathbf{r}_N \times \exp[-\mathcal{U}(\mathbf{r}_1, \mathbf{r}_2, \mathbf{r}_3, \ldots, \mathbf{r}_N)/kT], \tag{6}$$

where $\Lambda = (h^2/2\pi mkT)^{1/2}$ is the de Broglie wavelength, $\mathbf{r}_i$ is the position of the center of molecule i and $\mathcal{U}$ is the total potential energy of interaction, *i.e.* the sum of all of the u_{aa} and u_{as} terms,

$$\mathcal{U}(\mathbf{r}_1, \mathbf{r}_2, \mathbf{r}_3, \ldots, \mathbf{r}_N) = \sum_{i<j} \sum_j u_{aa}(r_{ij}) + \sum_i u_{as}(z_i) + \sum_i u_{as}(H - z_i). \tag{7}$$

If $u_{aa}(r) = \varepsilon_{aa} f(r^*)$ and $u_{as}(z) + u_{as}(H - z) = \rho_s \sigma_{as}^2 \Delta \varepsilon_{as} g(z^*, H^*, \frac{\sigma_{as}}{\sigma_{aa}})$, where f and g are universal functions for the systems considered, then

$$\mathcal{U}(\mathbf{r}_1, \mathbf{r}_2, \mathbf{r}_3, \ldots, \mathbf{r}_N) = \varepsilon_{aa} \sum_{i<j} \sum_j f(r_{ij}^*) + \rho_s \sigma_{as}^2 \varepsilon_{as} \Delta \sum_i g(z_i^*, H^*, \sigma_{as}/\sigma_{aa}), \tag{8}$$

where $r_{ij}^* = r_{ij}/\sigma_{aa}, r_{ij} = |\mathbf{r}_j - \mathbf{r}_i|$ and $H^* = H/\sigma_{aa}$ is reduced pore width. Here σ_{aa} and σ_{as} are parameters representing the molecular diameter for the *aa* and *as* interactions, respectively. The second term on the right in equation (8) is consistent with equations (3) and (4). On substitution of equation (8) in (6), the grand partition function can be written in terms of dimensionless variables as

$$\Xi = \sum_{N \geqslant 0} \frac{e^{N\mu^*/T^*}}{N! (h^{*2}/T^*)^{3N/2}} \int_0^{V^*} \cdots \int_0^{V^*} d\mathbf{r}_1^* d\mathbf{r}_2^* d\mathbf{r}_3^* \ldots, d\mathbf{r}_N^* \times \exp\left[-\frac{1}{T^*} \left(\sum_{i<j} \sum_j f(r_{ij}^*) + \alpha_w \sum_i g(z_i^*, H^*, \sigma_{as}/\sigma_{aa}) \right) \right], \tag{9}$$

where $\mu^* = \mu/\varepsilon_{aa}, T^* = kT/\varepsilon_{aa}, V^* = V/\sigma_{aa}^3$, $h^* = h/(2\pi m \varepsilon_{aa} \sigma_{aa}^2)^{1/2}$, $d\mathbf{r}_i^* = d\mathbf{r}_i/\sigma_{aa}^3$, and $H^* = H/\sigma_{aa}$. The *miscroscopic wetting parameter*, α_w, is given by

$$\alpha_w = \rho_s \sigma_{as}^2 \Delta(\varepsilon_{as}/\varepsilon_{aa}). \tag{10}$$

Examination of equation (9) and substitution into (5) shows that the grand free energy is a function of 6 variables,

$$\Omega = \Omega(\mu^*, T^*, V^*; \alpha_w, H^*, \sigma_{as}/\sigma_{aa}). \tag{11}$$

Since the chemical potential is constant, it is related to the bulk phase variables via an equation of state, $\mu^* = \mu^*(T^*, P_{bulk}^*)$. It is therefore convenient to replace the chemical potential by the experimental variable, bulk phase pressure, in equation (11),

$$\Omega = \Omega(P_{bulk}^*, T^*, V^*; \alpha_w, H^*, \sigma_{as}/\sigma_{aa}). \tag{12}$$

The reduced total volume, V^*, appears in equation (12) because the grand free energy is an extensive property. We shall be concerned primarily with intensive properties, including the local densities and compositions, local pressure, specific adsorption and isosteric heats. For such properties, the volume is no longer a variable and, for some point property, b, equation (12) becomes

$$b = b(P_{bulk}^*, T^*; \alpha_w, H^*, \sigma_{as}/\sigma_{aa}). \tag{13}$$

The first two independent variables, P_{bulk}^* and T^*, are the usual *state variables* for the bulk phase that is in equilibrium with the confined phase. The three new *system variables*, $\alpha_w, H^* and \sigma_{as}/\sigma_{aa}$, are needed to describe the nano-scale confinement. In the limit $H^* \to \infty$ we recover the bulk phase. Thus, as H^* is decreased, we can expect the effects of confinement to increase; qualitative behavior of the confined phase can also occur due to changes in the pore width, for example phase change from a gas-like to a liquid-like, or from liquid-like to solid confined phase, as has been observed in surface force apparatus experiments [9–11]. Provided that the adsorbate molecules are relatively rigid, the diameters σ_{aa} and σ_{as} are not very different and the pore width comfortably exceeds the diameter of the adsorbate molecules, the size ratio, σ_{as}/σ_{aa}, is found to have only a minor effect on the confined nano-phase [12], and in such cases is sometimes neglected, so that equation (13) simplifies to

$$b = b(P_{bulk}^*, T^*; \alpha_w, H^*). \tag{14}$$

The microscopic wetting parameter α_w is the ratio of the attractive interaction between an adsorbate molecule and the wall relative to that between two adsorbate molecules, and is thus a measure of the degree to which the adsorbate wets the wall. For adsorbates such as nitrogen or hydrocarbons on carbon walls, α_w is large and these adsorbates wet such walls easily; conversely, for adsorbates such as water or mercury on carbon walls, for which the adsorbate–adsorbate interactions are strongly attractive, α_w is small and only partial wetting, or non-wetting occurs. For macroscopic systems, the contact angle, θ_c, of a drop of liquid on the solid surface is often used as a measure of wetting. It has been shown that such contact angle measurements correlate closely with the values of α_w for surfaces such as graphite, silica and mica [13]. Thus, $\alpha_w = 0$ (complete non-wetting) corresponds to $\theta_c = 180°$, while large values of α_w (wetting) correspond to small θ_c values. As shown in what follows, α_w greatly influences the qualitative nature of confinement effects.

Equation (3), and hence the function b in equation (14), are appropriate for slit-shaped pores. However, analogous adsorbate-wall equations can be derived for pores of cylindrical or spherical shapes [14]. For these pore geometries, equation (14) remains unchanged, with the exception that H^* is replaced by $R^* = R/\sigma_{aa}$, where R is the pore radius. However, the functional dependence of b on the dimensionless pore width and wetting parameter shown on the right-hand side of equation (14) will differ for the different geometries.

The analysis given here omits many other factors that can be important for certain systems or properties, for example, non-central intermolecular interactions, pore shape, geometric and chemical 'roughness' of the pore walls, connectivity and tortuosity of pores. Nevertheless, the principal variables considered here will be important for all nano-confined systems, and this simple analysis provides a useful framework for the discussion below. The influence of additional factors will be discussed where needed.

3. Properties of confined phases (examples)

3.1. Phase changes and adsorption

Confinement results in shifts in the bulk system phase boundaries of (gas + liquid), (liquid + solid), (gas + solid) and (solid + solid) transitions in the case of pure substances, and (liquid + liquid) and '(gas + gas)' transitions for mixtures. In addition, new surface- and confinement-driven phase changes can occur, including layering transitions on atomically flat surfaces, hexatic phases and new solid phases. Experimental methods for the study of such phase changes include adsorption isotherm measurement, differential scanning calorimetry, dielectric relaxation spectroscopy, positron annihilation and X-ray and neutron diffraction. The main theoretical tools have been classical density functional theory and molecular simulation, particularly grand canonical Monte Carlo methods. In the case of experimental studies, because the porous materials often have a range of pore sizes and some surface roughness, the phase transitions are usually somewhat 'blurred', whereas in theoretical studies the model materials can have perfect pores of equal size and with smooth walls, so that sharp transitions are then often seen. The effects of confinement on phase transitions has been the subject of reviews [15–17].

For two-phase equilibrium in the pore we have one less degree of freedom, so that for the reduced phase transition temperature, T^*_{tr}, equation (14) becomes:

$$T^*_{tr} = T^*_{tr}(P^*_{bulk}; \alpha_w, H^*). \quad (15)$$

In figure 2 is shown the pressure–temperature phase diagram for carbon dioxide in Vycor glass, with average pore diameter of approximately 4 nm, as determined by positron annihilation [18,19]. The phase diagram for bulk CO_2 is shown for comparison. The (vapor + liquid) coexistence curve, PC, is seen to occur at a lower pressure than for the bulk material (capillary condensation), while the (liquid + solid) curve, PF, lies at temperatures about 12 K lower than for the bulk. For pressures below about 0.26 MPa, only a single transition is seen, which is believed to be the (solid + gas) sublimation. The results suggest that there is a pore triple point, PT, that lies about 10 K and over 0.2 MPa below the temperature and pressure of the bulk triple point, BT. We note that the system CO_2/Vycor has a relatively small value of α_w, *i.e.* carbon dioxide only weakly wets the walls. As shown below, for strongly wetting systems the behavior can be qualitatively different, with increases in the melting temperature and bulk pressure corresponding to (gas + liquid) equilibrium due to confinement, *i.e.*, the opposite of that shown in figure 2.

A subsequent X-ray diffraction study of the CO_2/Vycor system showed that at lower temperatures the confined solid had the same crystal structure as the bulk solid, but with a slightly larger lattice constant, with the solid in the pores being present as small crystallites [20]. This study is unusual in that substantial regions of the (gas + solid), (liquid + solid) and (vapor + liquid) were explored. An interesting feature of the phase diagram in figure 2 is that the freezing temperature of the confined nanophase is strongly affected by the bulk pressure in the range 0.27 MPa up to about 0.6 MPa. This is in strong contrast to the freezing behavior in the bulk phase, for which the freezing temperature is almost independent of pressure. We comment on the reason for this difference in Section 3.2.

3.1.1. The gas–liquid transition

(Vapor + liquid) condensation in pores, often referred to as *capillary condensation*, has been studied extensively. Adsorption isotherms for xenon in Vycor glass are shown in figure 3(a) as determined by Everett and coworkers [21] for a range of temperatures as a function of the fugacity, f, of the bulk gas. The Vycor used has pores that are roughly cylindrical, and while tortuous and interconnected the pore width is narrowly distributed, with a mean width of about 5 nm. The adsorption isotherms exhibit a low pressure region that is reversible (the curve is the same for increasing and decreasing gas pressure) followed by a rapid increase in adsorption over a narrow range of pressures. For temperatures of 242 K and below, this sharply rising region is accompanied by a hysteresis loop, with the curve for increasing pressure occurring at a higher bulk pressure than that for decreasing pressure. These steeply rising adsorption regions correspond to capillary condensation in the pores, and the hysteresis loop is a signature of such condensation in mesopores (pores with widths in the range (2 to 50) nm). As temperature is increased, the capillary condensation pressure increases and the hysteresis loops become narrower, until they disappear at some *hysteresis critical temperature*. The hysteresis loops represent metastable states in general,

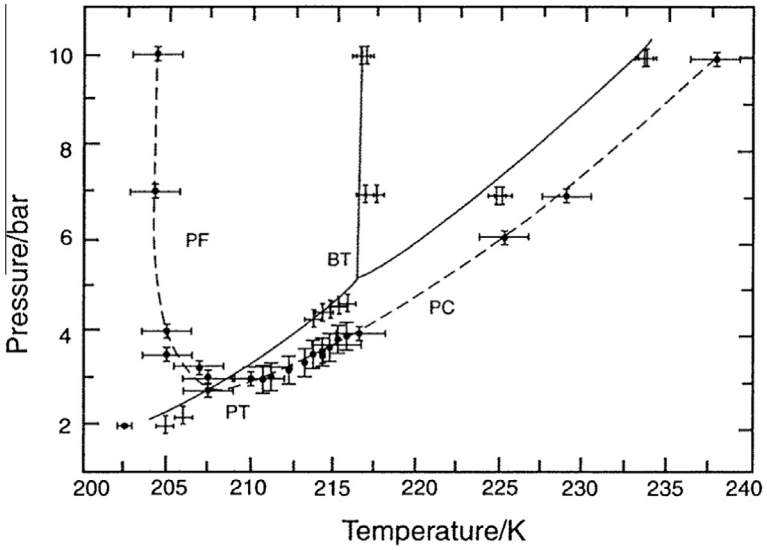

FIGURE 2. The phase diagram for carbon dioxide in the bulk phase (solid lines and + symbols) and in Vycor glass (solid symbols and dashed lines; the latter are a guide to the eye). Here B = bulk, P = pore, C = condensation, F = freezing, T = triple point. The pressure plotted on the vertical axis is that for the bulk phase in equilibrium with the pore phase. For this system, $\alpha_w = 1.5$. Adapted from reference [18].

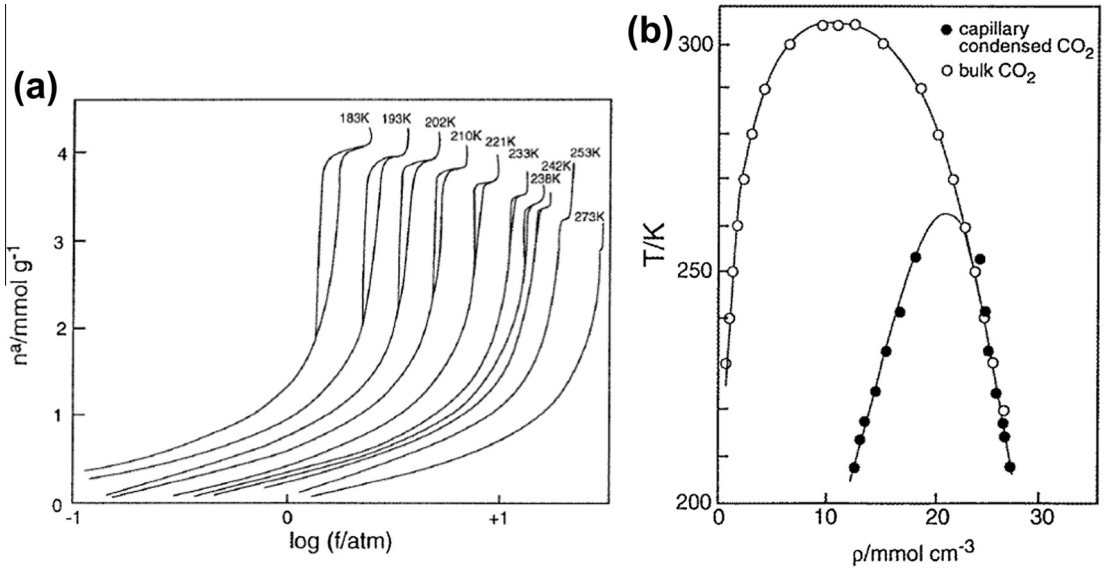

FIGURE 3. (a) Adsorption isotherms for Xe in Vycor glass, millimoles adsorbed per g of adsorbent *vs.* log of fugacity of Xe in the bulk gas phase. (b) Hysteresis phase diagram of CO_2/Vycor ($\alpha_w = 1.5$), compared with the (gas + liquid) phase diagram for bulk CO_2. Reproduced with permission from reference [21].

and so the hysteresis critical temperature may not be the same as the true (gas + liquid) critical temperature in the pore.

A *hysteresis phase diagram* can be constructed by plotting the temperature *vs.* the number of moles adsorbed (or average density in the pores) at the extreme ends of the hysteresis loops. Such a diagram is shown in figure 3(b) for CO_2 in Vycor, and superficially resembles the equilibrium (vapor + liquid) phase diagram for the bulk fluid, which is also shown for comparison. The hysteresis critical point is considerably lower than the bulk phase critical point, as expected by simple mean field theory [22], which predicts $T_c = cz\varepsilon/k$, where c is a constant, z is the mean coordination number of an adsorbate molecule, and ε is the interaction energy between neighboring adsorbate molecules; this lowering of the critical point on confinement can be thought of as occurring due to the reduced coordination number for the confined molecules. The curve for the 'gas-like' phase in the pore occurs at much higher densities than for the bulk phase diagram. This is because the confined phase consists of one or several layers of CO_2 adsorbed on the walls at high density, with gas-like densities in the interior of the pore; the total moles adsorbed is the sum of these high and low density regions.

In principle, it is possible to calculate the grand free energy of the system, and thus determine the true (vapor + liquid) equilibrium curve for the confined phase [23]. This can be done by making use of the thermodynamic relationships

$$\left(\frac{\partial\Omega}{\partial\mu}\right)_{T,V,H} = -\langle N\rangle, \tag{16}$$

$$\left(\frac{\partial(\Omega/T)}{\partial(1/T)}\right)_{\mu,V,H} = \langle U\rangle - \langle N\rangle\mu, \tag{17}$$

where $\langle N\rangle$ and $\langle U\rangle$ are the average number of molecules and average energy (internal energy), respectively. To determine the grand free energy a series of experiments over a range of temperatures (at constant chemical potential, *i.e.* bulk pressure) and over a range of chemical potentials (bulk pressures) at constant temperature would be required, connecting the state condition of interest to one where the grand free energy is independently known. The latter is usually the ideal gas state. Such a procedure would be very laborious, and as far as we know has not been attempted in experiments. However, it has been carried out in molecular simulation studies (*e.g.*, [23]).

Numerous studies have been made of phase coexistence in model pores, using either molecular simulation (usually grand canonical Monte Carlo) or classical density functional theory (DFT). Results from DFT calculations for an adsorbate modeled as methane in slit-shaped graphitic pores are shown in figure 4 [24]. (Vapor + liquid) coexistence (capillary condensation) curves are shown for three pore widths. Also shown are coexistence curves for two layering transitions which are observed in the larger pores. Layering transitions can occur on atomically flat walls for lower temperatures, and consist of a first order transition from a partially formed adsorbed layer to a fully occupied layer. This appears as a sudden step in the adsorption isotherm. A succession of layering transitions to form the first, second, third, *etc.* layers is possible, each with its own coexistence curve and critical point. Such transitions have been observed in both experiments and simulations for smooth surfaces such as graphite [15]. Surface roughness, however, breaks up the layers and such transitions then do not usually occur.

In the examples given so far, the wetting parameter α_w is greater than unity, indicating that the confined phase wets the walls; in such cases condensation in the pores occurs at pressures well below the bulk vapor pressure (capillary condensation). For non-wetting systems having much smaller α_w values, it is possible to observe *capillary evaporation*, *i.e.* condensation occurring at pressures above the normal vapor pressure. Examples include water ($\alpha_w \sim 0.5$) or liquid mercury ($\alpha_w \sim 0.1$) on carbon surfaces.

While the results shown in figure 4 are for slit-shaped pores (a simple model for many porous carbons), porous silicas and oxides, as well as some carbons have pores that are approximately cylindrical. Adsorbates in cylindrical pores exhibit two main differences from their behavior in slit pores. First, the adsorbate is confined in two dimensions in the case of cylinders, rather than one as in slit pores, and so the confinement effects are larger. Thus, for a given pore width and material, capillary condensation occurs at lower pressures in cylindrical pores. Second, for narrow cylinders the system approaches a one dimensional limit, and so cannot show true phase transitions at temperatures above 0 K. As a result, first order phase transitions in cylindrical pores are rounded due to finite size effects [25]. However, except for extremely narrow pores this

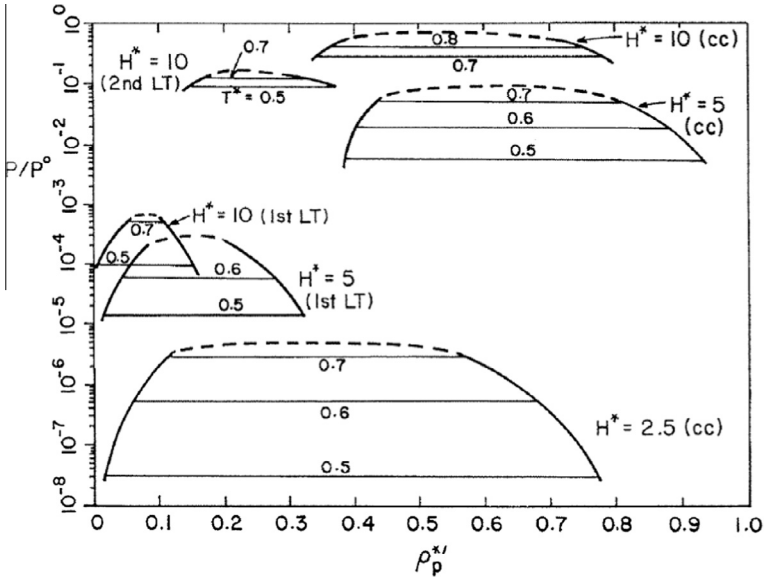

FIGURE 4. Equilibrium phase coexistence envelopes for a system modeled on methane in slit-shaped graphitic pores ($\alpha_w = 2.16$), as calculated by DFT. Here P is bulk phase pressure, P^o is vapor pressure of methane, and $\rho_p^{*\prime} = \rho_p' \sigma_{aa}^3$ where ρ_p' is the number density in the pore excluding the dead space near the walls. Dashed curves are a rough estimate of the pore critical region. Numbers on the tie lines are the reduced temperature, T^*. Reproduced with permission from reference [24].

effect has been found to be small. Thus for pores of radius $R/\sigma \sim 2.5$ capillary condensation transitions appear sharp in both molecular simulations and DFT calculations [26,27].

3.1.2. The liquid–solid transition

For a nano-scale liquid drop or solid nanoparticle the melting temperature, T_m, is lowered relative to that for the bulk material, because molecules near the surface have a lower coordination number than in the bulk. Early experiments also showed a decrease in the melting temperature on confinement in porous solids, and it was widely assumed that such a depression would always occur for confined nano-phases. However, these early experiments were for silica and oxide materials, for which the wetting parameter is rather small, $\alpha_w \sim 0.5$–1.2. More recent experiments and simulations on carbons and mica materials, for which the wetting parameter can be considerably larger, *e.g.* $\alpha_w \sim 2.0$–2.5, show a significant increase in the melting temperature. The situation for a confined nano-phase is quite different from that for a drop or nanoparticle, since there can be strong interactions between adsorbate molecules near the wall and the wall itself. The magnitude of these shifts in the melting temperature depends on the pore width, H^*, usually becoming larger as H^* decreases.

The first experiments to suggest an increase in T_m on confinement were made using the surface force apparatus (SFA), in which the nanophase is confined between two atomically smooth mica surfaces [28,29]. The pore is essentially slit-shaped and the pore width H can be finely controlled; both the normal and shear (on sliding one mica surface relative to the other) forces due to the confined nano-phase can be measured. Such studies performed by Klein and Kumacheva [10] for the globular molecules octamethylcyclotetrasiloxane (OMCTS, $\sigma_{aa} \sim 0.9$ nm) and cyclohexane ($\sigma_{aa} \sim 0.55$ nm) at room temperature showed strong support for a liquid → solid transition as the pore width was decreased. For OMCTS this transition occurred as pore width was reduced from 7 → 6 molecular layers, while for cyclohexane the transition occurred as width was reduced from 8 → 7 layers [10,30]. The transitions were reversible, the liquid-like phase being recovered on increasing the pore width. Similar transitions on decreasing H have been observed for toluene [10] and n-alkanes [29,31] using the SFA. Molecular simulation results for some of these systems, particularly by Cummings and coworkers [11,32,33], are in agreement with these experiments, and show a first order liquid → solid transition as the pore width is decreased. Although these simulations include recent free energy calculations [33] confirming the first-order transition, there remains some controversy [34], with some workers [35,36] arguing that the transition is second-order.

Numerous experimental and simulation studies have been reported, and these have been reviewed up to 2005 [16]. These, and more recent studies [37–43], show both an increase and a reduction in the normal melting point on confinement, the sign of the shift depending on the system and in particular on the value of α_w. A selection of recent experimental results are shown in figure 5, obtained by differential scanning calorimetry and dielectric relaxation spectroscopy, by Śliwinska-Bartkowiak and coworkers. These results show clearly the important role of both the pore width and wetting parameter. As the pore width H decreases the shift in the melting temperature increases, while the value of the wetting parameter α_w determines the sign of the shift, as well as its magnitude. For sufficiently large pores the shift in the melting temperature is linearly related to the inverse pore width according to the Gibbs–Thomson equation of thermodynamics:

$$\Delta T_m = T_{m,pore} - T_{m,bulk} = -2\frac{(\gamma_{ws} - \gamma_{wf})v}{H\lambda_{m,bulk}}, \tag{18}$$

where γ_{ws} and γ_{wf} are the wall–solid and wall–fluid surface tensions (here solid refers to the solid phase of the adsorbate), v is the molar volume of the liquid phase, and $\lambda_{m,bulk}$ is the bulk latent heat of melting. As seen from figure 5 this equation fails for pores much smaller than 10 nm in width for the systems considered. Such breakdown for narrow pores is expected, since the equation rests on macroscopic concepts such as surface tension (implying a well-defined interface between two bulk-like phases) and fails to account for the inhomogeneity of the confined phase.

Molecular simulation studies of the melting/freezing transition in nanopores show results similar to those in figure 5. In the simulations, it is possible to determine the structure of the confined phase, both directly by observing the atomic and molecular positions and configurations, and through the calculation of molecular correlation functions and structural order parameters. The Landau

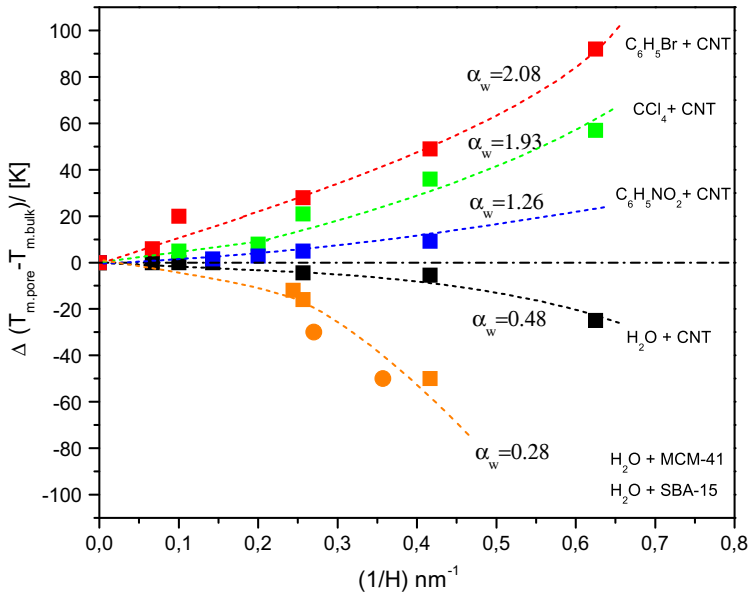

FIGURE 5. Experimentally measured [38,40–42] shifts in the melting temperature for confined nano-phases, showing the effect of pore width and wetting parameter. Here CNT = multi-walled carbon nanotube. MCM-41 and SBA-15 are silica materials.

theory of phase transitions [44–46], in which the Landau free energy $\Lambda(\Phi)$ is characterized by one or more order parameters Φ, is a convenient framework for use in theory and simulation studies of phase changes and stability in nano-confined phases, particularly if solid phases are present. It was first used to study solid–fluid transitions by van Duijneveldt and Frenkel [47]. The order parameters Φ are chosen so that they take on distinctly different values for different phases of the system. In the simulation, the probability density, $P(\Phi)$, of observing order parameter values between Φ and $\Phi + d\Phi$ is calculated. The Landau free energy is then given (within a constant) by:

$$\Lambda(\Phi) = -kT \ln[P(\Phi)], \tag{19}$$

and the grand free energy, Ω, is given by

$$\Omega = -kT \ln \int d\Phi \exp\left[-\frac{1}{kT}\Lambda(\Phi)\right]. \tag{20}$$

For simple quasi-spherical molecules, the two dimensional order parameter, Φj, introduced by Mermin [48] is appropriate for the study of the fluid–solid transition for an adsorbed layer j,

$$\Phi_j(\mathbf{r}) = \frac{1}{N_b}\sum_{k=1}^{N_b} \exp(i6\theta_k), \tag{21}$$

where θ_k are the imaginary bond angles between the molecule and it's nearest neighbors and the index k runs over the total number, N_b, of nearest neighbor bonds. The overall order parameter, Φ, is an average of the order over all adsorbed layers, $\Phi = \sum_j |\Phi_j|/N_{layers}$, and takes the value 0 when all the layers have the structure of a two-dimensional liquid and the value 1 for a two-dimensional face centered cubic solid phase, while other phases have intermediate values of Φ.

It is usually sufficient to calculate for each adsorbed layer, j, the radial distribution function, $g_j(r)$, giving the relative probability of finding two adsorbate molecules separated by distance r, and the bond orientational pair correlation function $G_{6j}(r)$ given by

$$G_{6j}(r) = \langle \Phi_j^*(0)\Phi_j(r)\rangle. \tag{22}$$

Typical results of this kind are shown in figure 6 for a Lennard–Jones model of methane in a slit-shaped carbon pore at two temperatures [39]. At the lower temperature the confined nanophase shows typical crystalline behavior, with long-ranged bond orientational order and positional order correlations, whereas at the higher temperature there is no long range orientational or positional order.

In addition to liquid-like and crystalline confined nanophases, under suitable conditions it is possible to observe surface-driven 'contact layer' phases, in which the layer of molecules in contact with the wall has a different structure from those in the interior of the pore. These contact layer phases are most easily observed in molecular simulations, where the pore walls can be atomically smooth, but there is also experimental evidence for their existence. In studies of a Lennard–Jones (LJ) model of methane in slit-shaped pores [12,49] it was found that for $\alpha_w < \sim 0.48$ the adsorbate-wall interaction was too weak to induce strong layering of the adsorbate, and only liquid-like and crystalline phases were observed (contact layer phases, when present, were metastable), but that

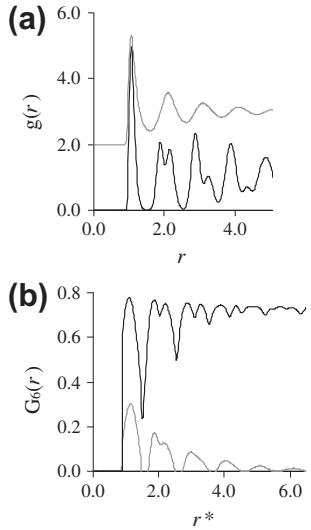

FIGURE 6. In-plane (a) 2D radial distribution function, and (b) 2D orientational pair correlation function for a model of methane confined at $P^* = 0.002$ in a slit carbon pore of width $H^* = 2$ at $T^* = 1.20$ (fcc crystalline phase, black lines) and $T^* = 1.58$ (liquid-like phase, gray lines). This narrow pore contains only one adsorbed layer of methane. Adapted from reference [39].

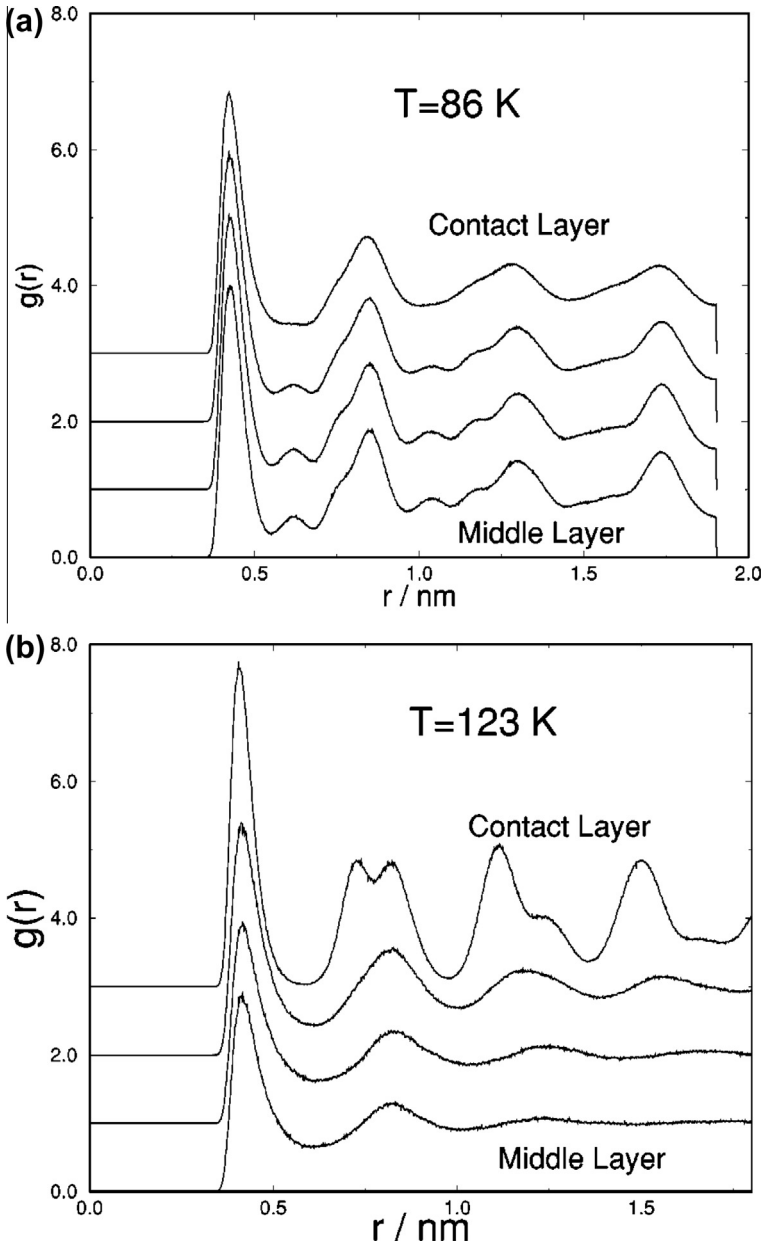

FIGURE 7. Two-dimensional in-plane radial distribution functions in the molecular layers for LJ methane in a slit pore: (a) weakly attractive pore walls, $\alpha_w = 0.68$, $T = 86$ K; (b) strongly attractive pore, $\alpha_w = 2.14$, $T = 123$ K. The curves for the various layers have been shifted upwards by one unit to aid in clarity. Reproduced with permission from reference [49].

for somewhat larger values of α_w (*e.g.* $\alpha_w = 0.68$) there was a range of temperatures over which a contact layer phase was observed in which the adsorbed layer in contact with the wall was liquid-like while the inner adsorbed layers were crystalline (see figure 7(a)). In such cases, the contact layer freezes at a lower temperature than the inner layers. For more strongly attractive walls, *e.g.* $\alpha_w = 2.14$ (the value for LJ argon on a graphite wall), the reverse situation is observed, the contact layer being crystalline while the inner adsorbed layers are liquid-like (see figure 7(b)). In this case the contact layer freezes at a higher temperature than the inner layers. There is considerable experimental evidence for such contact layer phases, for the contact liquid layer phase in silica pores [50–52] and for the contact crystal phase in carbon pores [53].

Landau free energy calculations in grand canonical Monte Carlo simulations can be used to calculate phase diagrams for confined systems. An example [12] is shown in figure 8, which shows the shift in freezing temperature in a slit pore of width $H^* = 7.5$, the adsorbate being composed of spherical Lennard–Jones molecules, and the bulk pressure being fixed at one atmosphere. Phase transition points were determined from the grand free energies [46], as given by equation (20), which when plotted *vs.* temperature showed various crossing points for the curves for the different phases. In addition to crystalline (C) and liquid-like (L) phases, three distinct contact layer phases were observed, depending on the range of wetting parameter values considered – a contact-liquid phase at small to moderate α_w, and both a contact-crystal and a contact-hexatic phase at higher α_w. While these contact layer phases are distinctly seen as resulting from first-order transitions in the molecular simulations, using model pores with atomically smooth walls, they prove more elusive in experimental studies, probably because wall roughness and defects tends to disturb the adsorbed contact layers.

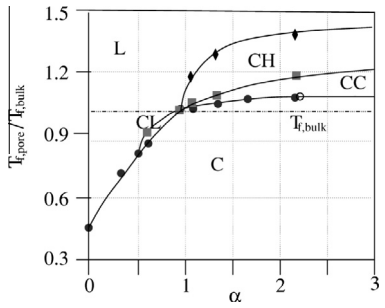

FIGURE 8. Global freezing diagram for a Lennard–Jones adsorbate in a slit pore of width H^* = 7.5 with the Steele 10-4-3 adsorbate-wall potential, for a bulk pressure of 1 atmosphere. The closed symbols are results of GCMC simulations in which the Landau free energy, and hence the grand free energy is calculated; lines through these points are two-phase lines where the phases shown are in equilibrium, and are a guide to the eye. The dash–dot–dot–dot horizontal line gives the value that the freezing temperature in the pore would have if no shift occurs, and is included for reference. Five different phases are observed: face-centered cubic crystal (C), liquid (L), contact-liquid (CL), contact-hexatic (CH) and contact-crystal (CC). The open circle is the experimental surface force apparatus result of Klein and Kumacheva [10] for cyclohexane in a mica slit pore of this width. Reproduced with permission from reference [12].

The simulation results discussed so far have been for slit-shaped pores. For cylindrical pores, having confinement in two dimensions rather than one, the freezing temperature is generally lower than for slit pores of the same width [51,54–60]. Both experiments and simulations (involving free energy calculations) suggest that for pore diameters smaller than $20\sigma_{aa}$ only partial crystallization occurs, and for even smaller pores the confined solid phase may be amorphous.

3.1.3. Mixtures

It is straightforward to extend the corresponding states analysis of Section 2.2 to a mixture of components 1,2,3,...,m. Equation (14) for some intensive property, b, becomes

$$b = b(P^*_{bulk}, T^*, x_{1,bulk}, x_{2,bulk} \ldots, x_{m-1,bulk}; H^*, \alpha_{w1}, \alpha_{w2} \ldots, \alpha_{wm}, \sigma_{aa2}/\sigma_{aa1}, \sigma_{aa3}/\sigma_{aa1}, \ldots, \sigma_{aam}/\sigma_{aa1}), \quad (23)$$

where it is implicitly assumed that unlike-pair adsorbate–adsorbate interaction parameters, σ_{ij} and ε_{ij}, are related to the like-pair parameters through some combining rule. We shall consider binary mixtures of components 1 and 2, for which equation (23) becomes

$$b = b(P^*_{bulk}, T^*, x_{1,bulk}; H^*, \alpha_{w1}, \alpha_{w2}, \sigma_{aa2}/\sigma_{aa1}). \quad (24)$$

There is thus one new state variable, the bulk mole fraction of component 1, and two new system variables, the wetting parameter for component 2 and the size ratio for the two adsorbate molecules.

In the case of mixtures, the important new feature is the difference in composition between the bulk and confined phases, and the consequent effect on phase equilibria. For a particular mixture component, i, this difference can be expressed as the partition coefficient between the two phases,

$$K_i = \frac{C_{i,pore}}{C_{i,bulk}} = \frac{\bar{x}_{i,pore} C_{pore}}{x_{i,bulk} C_{bulk}}, \quad (25)$$

where $C_{i,pore}$ and $C_{i,bulk}$ are the overall mole concentrations of component i in the pore and bulk phases, respectively, C_{pore} and C_{bulk} are the total mole concentrations in the two phases, and $\bar{x}_{i,pore}$ *and* $x_{i,bulk}$ are the overall mole fraction of i in the pore and bulk phases. Within the pores the local mole fraction, $x_{i,pore}(\mathbf{r})$, will vary strongly with position $\mathbf{r}$, and $\bar{x}_{i,pore}$ is the average of $x_{i,pore}(\mathbf{r})$ over the pore volume. The extent to which the porous material favors the adsorption of component i over a component j is described by the selectivity S_{ij},

$$S_{ij} = \frac{(\bar{x}_{i,pore}/\bar{x}_{j,pore})}{(x_{i,bulk}/x_{j,bulk})} = \frac{K_i}{K_j}, \quad (26)$$

and is of particular relevance for mixture separations based on adsorption. In addition to these changes of composition within the pore, phase equilibria for the mixture can be affected. For example, ethanol and water are miscible at all concentrations in the bulk liquid at ambient temperature, but experimental studies suggest that two immiscible liquid phases may form in nanopores [61]. For other systems with two immiscible bulk liquid phases the mixture may be fully miscible at all concentrations in the pore [62].

The selectivity depends strongly on temperature, pore width, and the difference between the potential well depths for the interaction with the wall for the two adsorbate components. Jiang *et al.* [63] used Kierlik–Rosinberg [64] non-local density functional theory to carry out a systematic study of the selectivity for a trace component, 2, in a Lennard–Jones methane solvent adsorbed into graphite slit pores of various widths. The fluid-wall potential was taken to be Steele's 10-4-3 model, equation (3). They calculated the selectivity at infinite dilution of the trace component (2), S^{∞}_{21}, and examined the influence of varying the temperature, bulk pressure, pore width and intermolecular potential parameters for the trace component for a range of values that embrace the main constituents of natural gas. Low temperatures (below the critical

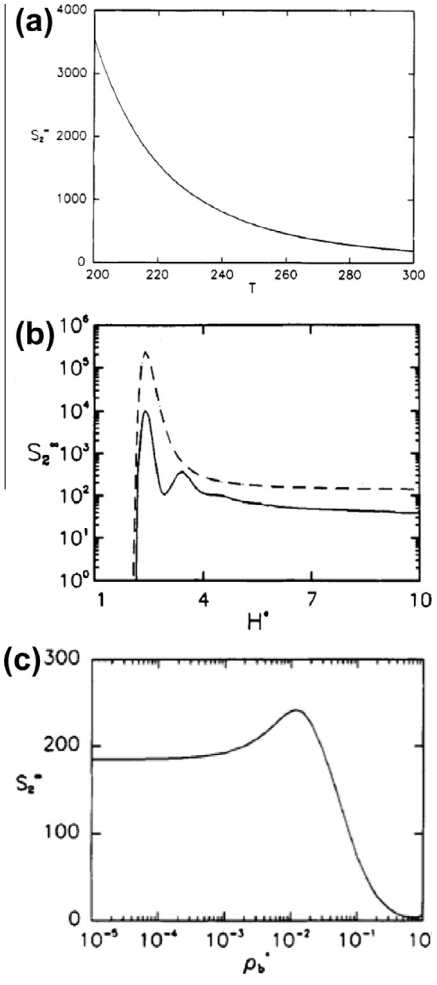

FIGURE 9. Effect of (a) temperature, (b) pore width and (c) bulk gas density on the selectivity for trace component 2 at infinite dilution for a LJ mixture modeled on methane (1)/propane (2) in a carbon slit pore of width H^* = 5. In figure (a) the bulk density is $\rho_b^* = 10^{-4}$, while in figure (b) the density is $\rho_b^* = 10^{-4}$ for the dashed curve and $\rho_b^* = 10^{-1}$ for the solid curve. In figures (b) and (c) the temperature is 300 K. Adapted from reference [63].

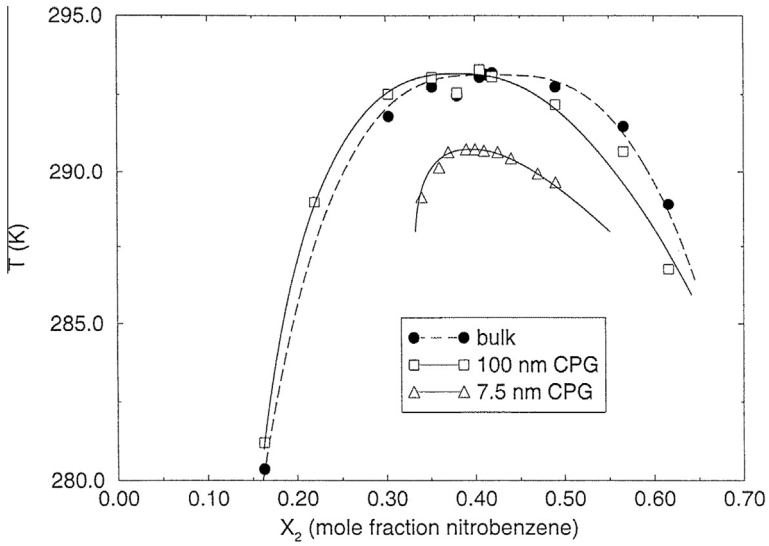

FIGURE 10. (Liquid + liquid) coexistence curves for mixtures of nitrobenzene with n-hexane confined within controlled pore glasses with pores of mean diameter (100 and 7.5) nm, compared with the bulk phase diagram. Reproduced with permission from reference [15].

temperature of the trace component), small pore widths and large potential well depth ratios $\varepsilon_{a2s}/\varepsilon_{a1s}$ all favored high selectivities.

Some typical results from this work are shown in figure 9. The selectivity values are large for this system, particularly at low temperatures, because of the relatively large difference in the adsorbate–adsorbate potential well depths for the two components. The selectivity decreases with temperature as kinetic energy increases, as expected. For low bulk densities, the selectivity increases smoothly as the pore width is reduced, reaching a maximum at a pore width that can comfortably accommodate a single layer of propane molecules. For smaller pore widths the pore becomes too narrow for the propane molecules to enter, and selectivity falls off steeply. For higher bulk densities, the selectivity oscillates with pore width for pore widths below $H^* \sim 6$ due to packing effects, which cause oscillations in the average density in the pore as H^* decreases. Figure 9(c) exhibits an interesting maximum in selectivity at a bulk density ρ_b^* of $1.2 \cdot 10^{-2}$. For lower densities, as density increases propane is preferentially adsorbed, leading to an increase in selectivity, but for densities above $1.2 \cdot 10^{-2}$ methane molecules start to replace propane and the selectivity falls. The density functional theory calculations shown in figure 9 agree well with Monte Carlo simulations [65] showing the same trends with bulk pressure, pore width, temperature and bulk phase mole fraction.

(Liquid + liquid) separation in pores has been the subject of considerable study [15,66–73] by both experiment and theory. In most cases reported, the composition range over which immiscibility occurs is reduced by the confinement, and the critical temperature is lowered. An example of such behavior is shown in figure 10 for mixtures of nitrobenzene ($\alpha_w = 0.78$) and n-hexane ($\alpha_w = 1.34$) in two controlled pore glasses, having mean pore diameters of (100 and 7.5) nm. The results suggest that the coexistence curve for the confined fluid shifts towards the side of the component with the larger value of α_w, n-hexane in this case. The results were obtained from non-linear dielectric effect measurements, and also from light transmission measurements, by Śliwinska-Bartkowiak and coworkers [15,68] and show the lowering of the consolute point and the reduction of the immiscibility region in the pores.

Density functional theory and molecular simulation calculations for Lennard–Jones mixtures with parameters chosen to produce (liquid + liquid) separation give qualitatively similar results to the experiments [68,69]. Examples of results from DFT calculations are shown in figures 11 and 12. In this system, the adsorbate-solid attraction is greater for component 1 than for component 2, and this leads to a shift of the (liquid + liquid) coexistence curve to the left in the diagram, that is to the 1-rich phase side. This in turn leads to a reduced solubility of component 2 in the 1-rich phase (by a factor of about 2 in the pore of width $H^* = 10$), and an increase of the solubility of 1 in the 2-rich phase (figure 12).

Several experimental and molecular simulation studies have been reported on the effect of confinement on the (solid + liquid) transition in binary mixtures [74,11,75–80]. Two examples of experimental results obtained by dielectric relaxation spectroscopy and differential scanning calorimetry are shown in figure 13. The system shown in figure 13(a) exhibits an azeotrope in the bulk phase at a mole fraction $x(C_6H_{12}) = 0.23$. When confined within the roughly slit-shaped pores of activated carbon fiber, with mean pore width of $H = 1.2$ nm, the (solid + liquid) coexistence region is shifted to higher temperatures and the azeotrope shifts to the cyclohexane-rich side with $x(C_6H_{12}) = 0.75$. The behavior for the confined system can be qualitatively understood as arising from the different values of the wetting parameter for the two

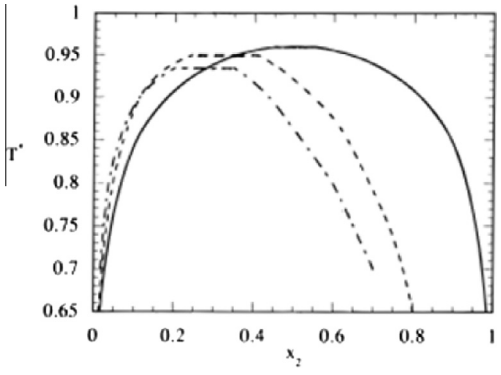

FIGURE 11. (Liquid + liquid) phase diagrams for a Lennard–Jones mixture at reduced pressure $P^* = 0.1$, with potential parameters $\varepsilon_{11} = \varepsilon_{22} = \varepsilon$, $\sigma_{11} = \sigma_{12} = \sigma_{22} = \sigma$; $\varepsilon_{12} = 0.8(\varepsilon_{11}\varepsilon_{22})^{1/2}$; $\varepsilon_{as1}/\varepsilon_{as2} = 1.2$, showing the bulk phase diagram (solid line) and the phase diagram for the mixture confined in slit-shaped carbon pores of width $H^* = 10$ (dotted-dashed line) and $H^* = 20.56$ (dashed line). Reproduced with permission from reference [68].

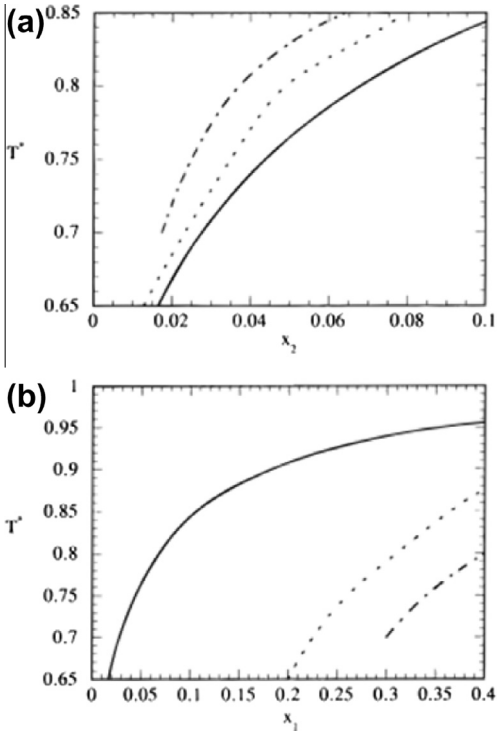

FIGURE 12. The effect of confinement on the solubility of the dilute component for the system of figure 11: (a) solubility of component 2 in the 1-rich phase; (b) solubility of component 1 in the 2-rich phase. Key as in figure 11. Reproduced with permission from reference [68].

components on carbon [78] $\alpha_w = 1.93$ for CCl_4 and $\alpha_w = 1.76$ for C_6H_{12}. These large values of α_w lead to the increase in the melting temperature for the mixture, and this increase is larger for CCl_4 than for C_6H_{12}, as expected (see figure 5). The azeotrope composition shifts towards the component having the smaller value of α_w, cyclohexane. It has been proposed [78] that such a shift in the azeotrope results from the larger increase in the melting temperature for the component having the larger value of α_w, carbon tetrachloride in this case. The mixture in figure 13(b), bromobenzene/carbon tetrachloride, exhibits a eutectic point at $x(C_6H_5Br) = 0.48$ for the bulk mixture. When confined within silica controlled pore glass, with mean pore width of $H = 7.5$ nm, the melting temperature is lowered relative to that in the bulk phase, and the eutectic composition shifts to $x(C_6H_5Br) = 0.70$. The lowering of the melting temperature is expected in view of the smaller values of the wetting parameter on silica surfaces for the two components ($\alpha_w \sim 1$ for both carbon tetrachloride and bromobenzene on silica [49]). Molecular simulation studies of the shift in the (liquid + solid) equilibrium due to confinement are in qualitative agreement with the experimental findings.

3.2. Pressure enhancement in pores

As noted in Section 2.1, due to the highly non-uniform nature of the confined nano-phase, the pressure **P** is a second-order tensor, having components $P_{\alpha\beta}$, β being the direction of the force and α the normal direction of the surface it acts upon. Provided that the system is not under stress the off-diagonal elements of **P** are zero, so that in Cartesian coordinates:

$$\mathbf{P} = \begin{pmatrix} P_{xx} & 0 & 0 \\ 0 & P_{yy} & 0 \\ 0 & 0 & P_{zz} \end{pmatrix}. \tag{27}$$

For the slit-shaped pore as shown in figure 1, with z being normal to the pore walls, we will have two pressures, that normal to the pore walls, P_N, and another parallel to the walls, P_T. Thus $P_{zz} = P_N$, the normal pressure, and $P_{xx} = P_{yy} = P_T$, the tangential pressure (we note that $P_{xx} = P_{yy}$ by symmetry). The condition of mechanical equilibrium, equation (2), for a slit pore becomes:

$$\left(\frac{\partial P_T}{\partial x}\right) = 0; \quad \left(\frac{\partial P_T}{\partial y}\right) = 0; \quad \left(\frac{\partial P_N}{\partial z}\right) = 0. \tag{28}$$

Thus the tangential pressure is independent of the values of x and y (but does depend on the distance, z, from the wall). The normal pressure is also independent of x and y, but in addition it is independent of the distance, z, from the wall. Thus for a given slit-shaped pore P_N is a constant everywhere in the pore space. For pores of cylindrical or spherical geometry the normal pressure does depend on the distance from the wall [81], and for cylindrical pores there are two tangential pressures, one in the direction parallel to the cylinder axis, and one in the direction of the azimuthal angle, ϕ.

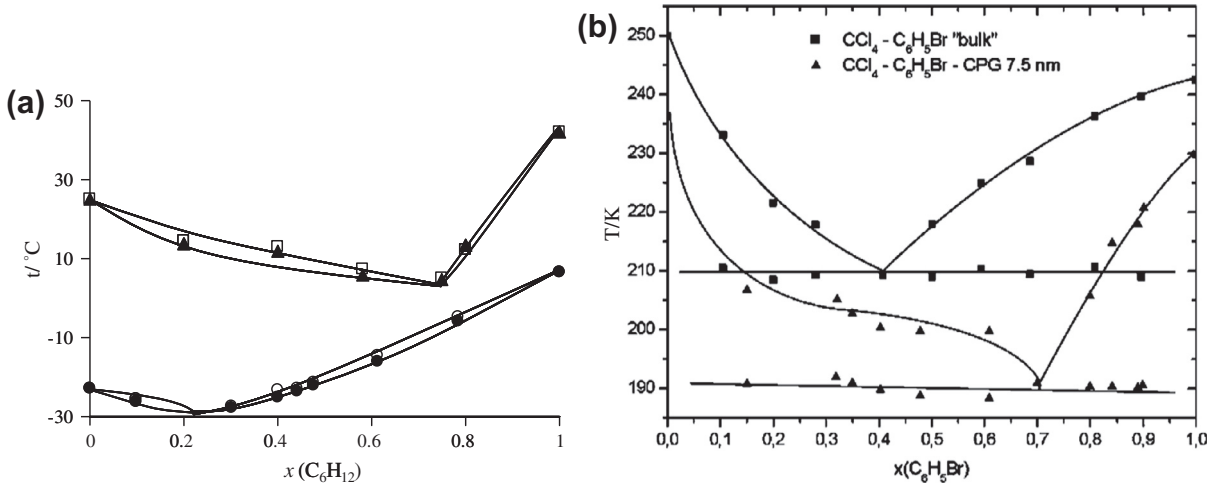

FIGURE 13. Experimental results showing the result of confinement on (solid + liquid) phase diagrams for binary mixtures. (a) carbon tetrachloride/cyclohexane at a bulk phase pressure of 1 atm., showing the phase diagram for the bulk mixture (circles) and for the mixture confined within activated carbon fibers with mean pore width $H = 1.2$ nm. Open and closed symbols denote the liquid and solid coexistence lines, respectively. (b) Bromobenzene/carbon tetrachloride at 1 atm bulk pressure; squares show the results for the bulk mixture, triangles are for the mixture confined within a silica controlled pore glass having a mean pore width of $H = 7.5$ nm. Lines connecting symbols are provided as a guide for the eye from references [78,79].

At present, we do not have a method to measure the tangential pressure experimentally. The normal pressure can be measured for some systems by using the surface force apparatus or atomic force microscope. Alternatively, it may be possible to estimate the normal pressure from changes to the solid structure of the adsorbent due to the adsorption of the confined nano-phase. Such changes may be observable from X-ray or neutron diffraction, and if the Young's modulus of the material is known the normal pressure acting on the pore walls can be estimated.

Despite the difficulty in measuring the pressures directly, there is much experimental evidence to suggest that the in-pore pressures can be very high. Examples include high pressure chemical reactions, high pressure solid phases, and high pressure effects in (solid + liquid) equilibria. We mention two such examples. The dimerization of nitric oxide, $2NO \rightleftharpoons (NO)_2$, is well-studied and is an example of a high pressure reaction that occurs in porous carbons at low bulk phase pressure. In activated carbon fibers (with an average pore width of 0.8 nm), the mole fraction of dimers is found to be 99% at $T = 300$ K and 0.1 MPa bulk pressure, as measured by magnetic susceptibility [82], while in the bulk gas phase at the same conditions the corresponding yield is less than 1 mol% dimer. Fourier transform infrared spectroscopy experiments [83] on this reaction in single-walled carbon nanotubes (1.35 nm in diameter) at somewhat lower temperatures similarly indicated ~100 mol% conversion to dimers. A simple thermodynamic calculation suggests that a bulk phase pressure above 1200 MPa is required to achieve a dimer conversion of (98 to 99) mole% at these temperatures in the bulk phase. In addition, phases that occur only at high pressure in the bulk material are often observed in nanopores. Thus, high-resolution transmission electron microscopy and synchrotron X-ray diffraction experiments [84] provided evidence that KI nanocrystals in single-walled carbon nanohorns (~2 nm diameter) exhibit the super-high-pressure B2 structure even though the pressure of the bulk phase was below 0.1 MPa. The B2 phase occurs only at pressures above 1900 MPa for bulk KI crystals.

Although experimental measurements are difficult at present, these pressures can be calculated in molecular simulations. There are at least two routes to the determination of the normal and tangential pressures in simulations, the virial route [4,85] in which one tracks the intermolecular forces and averages them, and the thermodynamic route [86] in which small volume changes are made by perturbing the length of the simulation box in a particular direction, α, and determining the pressure $P_{\alpha\alpha}$ from the thermodynamic identity

$$P_{\alpha\alpha} = \lim_{\Delta V \to 0} \left(\frac{\Delta A}{\Delta V} \right)_{N,T,\beta \neq \alpha}, \tag{29}$$

where A is the Helmholtz energy.

3.2.1. The normal pressure

Although the pressure in the direction normal to the pore walls is constant for a given slit-pore, it depends strongly on the pore width, and oscillates as H increases due to molecular packing effects. This is illustrated in figure 14 for argon and carbon tetrachloride confined within slit carbon pores. The results are presented in terms of the 'effective pore width', $H' = H - \sigma_{CC}$, to allow for the dead space near the pore walls. The inverted triangles and solid circles are results from Grand Canonical Monte Carlo (GCMC) simulations [85,87], while the single diamond point is from experiment [87] for CCl_4 in activated carbon fibers (ACF). The oscillations in the normal pressure arise from oscillations in the average density in the pore as H increases. Thus, for $H'^* = 1.8$ the pore can accommodate two complete layers of adsorbate, but further increase in pore width to $H'^* \sim 2.3$ is necessary before a third layer can begin

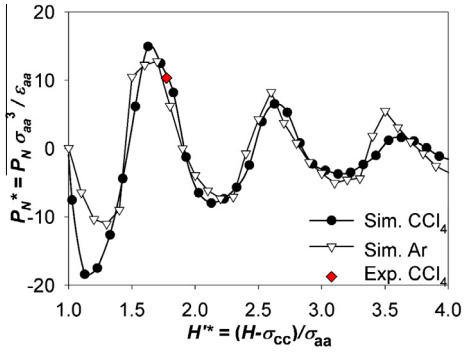

FIGURE 14. The normal pressure as a function of pore width for Lennard–Jones models of argon at $T = 87.3$ K and 0.1 MPa bulk pressure, and carbon tetrachloride at $T = 300$ K and 0.1 MPa bulk pressure, in slit-shaped carbon pores. The single experimental point [87] for CCl_4 was obtained from X-ray diffraction measurements on activated carbon fibers having a mean pore width of 1.4 nm.

to form. For pore widths in the range (1.8 to 2.3) the average density in the pore falls, and the normal pressure falls with it. Once the third layer starts to form, the density and normal pressure increase rapidly, until the third layer is complete at about $H'^* \sim 2.6$. The amplitude of the oscillations in P_N are of the order a few hundred MPa for the smaller pore widths. Such oscillations have been observed [88] in surface force experiments. Similar oscillations are observed in simulations for cylindrical and spherical pores [89].

The experimental point in figure 14 was obtained from X-ray diffraction measurements of Δd_{002}, the change in d_{002} due to the adsorption, where d_{002} is the separation distance between the graphene layers in the activated carbon fibers. Using Young's equation, $P_N = -E_T(\Delta d_{002}/d_{002})$, where E_T is the transverse compressive modulus of the ACF, the normal pressure can be estimated to be (+345.2 ± 170.0) MPa; the rather large error bar is due to the uncertainty in the value of E_T for the ACF.

The influence of the wetting parameter on the normal pressure is shown in figure 15 for several pore widths. In these calculations, the wetting parameter was varied by varying the potential well depth, ε_{ww} (and hence ε_{aw}), for the interaction among wall atoms keeping ε_{aa} constant. The unlike pair potential parameters were obtained from the Lorentz-Berthelot combining rules, $\sigma_{aw} = \frac{1}{2}(\sigma_{aa} + \sigma_{ww})$ and $\varepsilon_{aw} = (\varepsilon_{aa}\varepsilon_{ww})^{1/2}$. The results reflect several effects. For H^* values of (3.0 and 7.0), several adsorbed layers fit readily into the pore, the normal force is, on average, attractive, *i.e.* negative; thus the normal pressure is negative and increases in magnitude as the wetting parameter is increased, the effect being greater for the smaller pore, as expected. The curve for $H^* = 2.0$ results from a change in the relative contributions from adsorbate–adsorbate forces (which are repulsive due to strong compression from the walls, hence positive contributions to P_N) and the adsorbate-wall forces, which are

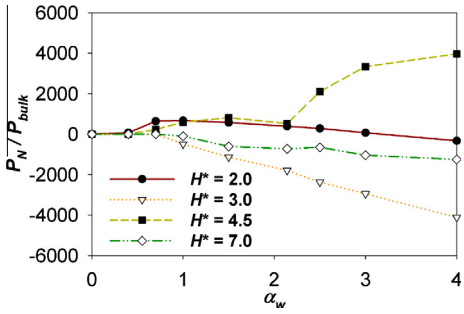

FIGURE 15. Normal pressure as a function of α_w for various pore widths for LJ argon at $T = 87.3$ K and 0.1 MPa bulk pressure.

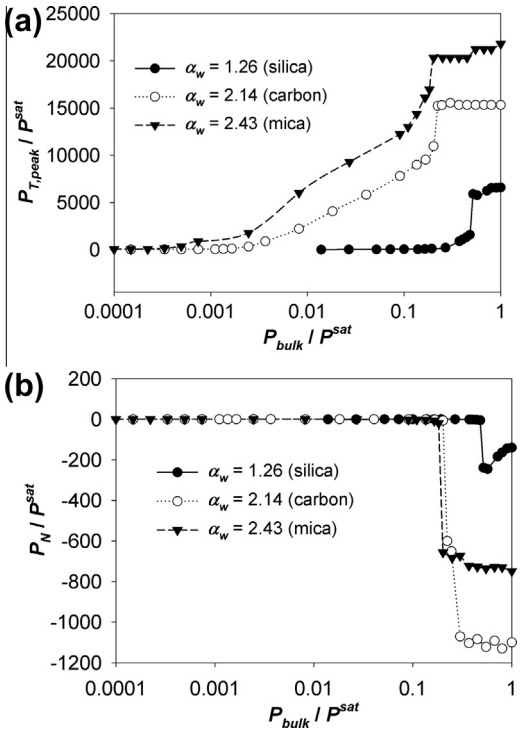

FIGURE 16. The effect of the bulk pressure on (a) the peak tangential pressure for the contact layer and (b) the normal pressure, for LJ argon at $T = 87.3$ K (the normal boiling point) in a slit pore of width $H^* = 7.0$, for various α_w values. The bulk pressure is P^{sat}, that is 0.1 MPa. The sharp jumps in the pressure occur at capillary condensation.

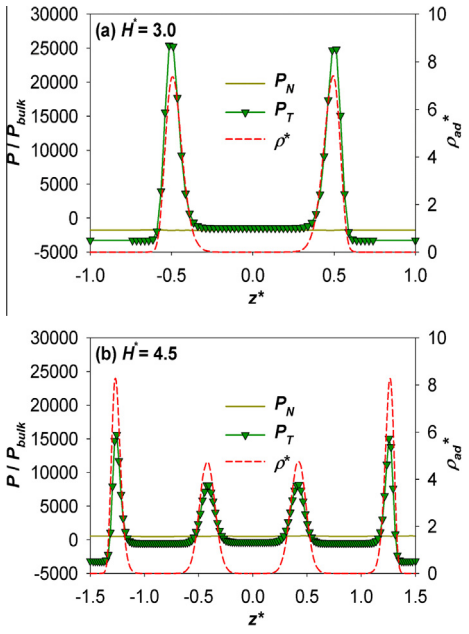

FIGURE 17. The local density, normal pressure and tangential pressure profiles for LJ argon at $T = 87.3$ K and 0.1 MPa bulk pressure in slit carbon pores having 10-4-3 walls of width (a) $H^* = 3.0$ and (b) $H^* = 4.5$.

negative, *i.e.* attractive. For small values of α_w there is little adsorption, but for $\alpha_w \sim 0.7$ an adsorbed layer forms and the positive adsorbate–adsorbate forces are strong relative to the negative adsorbate-wall forces, leading to a positive normal pressure. As α_w increases further, however, the contribution of the negative adsorbate-wall forces becomes increasingly important, and the normal pressure starts to decrease and eventually becomes negative. For $H^* = 4.5$ the normal pressure becomes positive at small and moderate α_w, as for $H^* = 2.0$, but when $\alpha_w \sim 2.2$ there is a transition to a solid crystalline phase, resulting in an increase in the density of the adsorbed layers, and a consequent increase in the positive value of the normal pressure.

The influence of the bulk pressure on the normal pressure in the pore is shown in figure 16(b) for a pore width of $H^* = 7.0$. In a pore of this width, capillary condensation occurs at a bulk pressure that depends on the temperature and on the value of α_w. The bulk pressure is seen to have very little influence on P_N for pressures below the capillary condensation point. However, capillary condensation results in a sharp change in P_N. For a pore width of 7.0, for which the adsorbed layers fit easily into the pore, P_N is negative (attractive force acting on the walls). For other pore widths P_N can be positive, and capillary condensation may then lead to a sudden increase in P_N.

3.2.2. The tangential pressure

In GCMC simulations, the local tangential pressure, $P_T(z)$, is calculated as a function of the distance z from the pore wall. Some typical results are shown in figure 17 for LJ argon in a slit carbon pore at the normal boiling point of argon, $T = 87.3$ K and 0.1 MPa bulk pressure. The local tangential pressure is seen to depend strongly on the local density, $\rho(z)$. As shown in figure 17, the tangential pressure in the center of the adsorbed contact layers next to the wall are very high, over 2500 MPa for $H^* = 3.0$ and over 1500 MPa for $H^* = 4.5$. In the case of the larger pore, two interior layers are formed and have lower pressures, although still of the order 800 MPa at the peak.

The effect of the wetting parameter and pore width on the tangential pressure is shown in figure 18. In this figure, the more physical average tangential pressure, $P_{T,avg}$, is plotted rather than the local pressure. The average tangential pressure is the unweighted average of the local pressure, *i.e.*,

$$P_{T,avg} = \int_{-H/2}^{+H/2} P_T(z)dz. \tag{30}$$

For very small values of α_w the tangential pressure becomes increasingly negative as the pore width is reduced, but this trend is reversed for $\alpha_w \geqslant \sim 0.5$, resulting in average tangential pressures of 1000 MPa or higher for small pores and $\alpha_w > \sim 2$. This behavior for the effect of α_w and inverse pore width on the tangential pressure from molecular simulation is similar to their influence on the experimental determined freezing temperature in the pore displayed in figure 5.

The influence of the bulk pressure on the tangential pressure is illustrated in figure 16(a) for pores of width $H^* = 7.0$. In contrast to

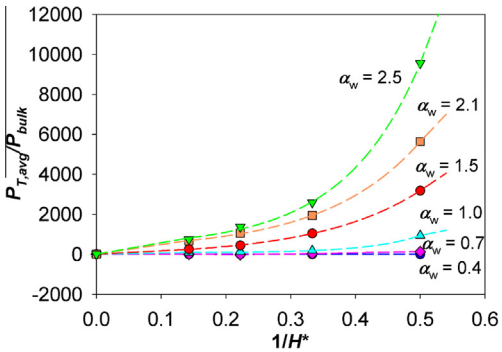

FIGURE 18. Average tangential pressure *vs.* inverse pore width for various α_w for LJ argon at its normal boiling point, $T = 87.3$ K and 0.1 MPa bulk pressure. In these calculations different α_w were obtained by varying ε_{ww} (and hence ε_{aw}), keeping ε_{aa} constant. The pore width H^* is measured in molecular diameters.

the normal pressure, for which the bulk pressure has very little effect below the capillary condensation pressure, the tangential pressure increases very rapidly with even very small increases in bulk pressure. This is especially noticeable for α_w values corresponding to carbon and mica walls, where the tangential pressure rises roughly exponentially once adsorption begins, until capillary condensation occurs. For the case of the carbon pore, for example, an increase in the bulk pressure of about one hundredth of a MPa, from P_{bulk} of (0.001 to 0.01) MPa, results in an increase in the peak tangential pressure of about 650 MPa. This suggests that variation of the bulk pressure in experiments might enable observation of a variety of phase transitions in the pore, making it possible to study the high pressure part of the in-pore phase diagram.

4. Conclusions

The simplified model treated here provides a useful framework for a qualitative understanding of many of the thermodynamic phenomena encountered in confined nano-phases. The two main system variables, pore width expressed as the number of molecular diameters, and the microscopic wetting parameter, α_w, emerge naturally from the corresponding states treatment, and aid in interpreting experimental data, such as capillary condensation and freezing transitions in pores (see, for example, figure 5). However, other factors, such as the roughness of the pore walls, their shape and connectivity, and non-spherical intermolecular interactions are not accounted for in this model, and can be important for certain properties. Wall roughness leads to heterogeneity of the adsorption sites and is known to have a strong effect on adsorption isotherms at low loading [90,91] and on the tangential pressures near the pore walls [81]; in the latter case the roughness disrupts the adsorbed contact layers next to the wall, lessening the compression of these layers. Adsorbates whose molecules associate, due to hydrogen bonding or other specific interactions, tend to form molecular clusters when confined, rather than regular layers. This is particularly the case for adsorbed water in carbon materials [92,93].

We have mainly considered slit-shaped pores. These are somewhat easier to treat since the confinement is in only one direction, and in the limit that pore width becomes very small the confined nanophase becomes two dimensional, and so still has well-defined phase transitions. Curved pore walls, as in cylindrical and spherical pores, leads to confinement in two or three dimensions, respectively, and stronger steric hindrance by the walls. In the limit of small pore width the confined nanophase becomes one- or zero-dimensional, respectively. In such pores phase changes are rounded, and will not occur for very small pores.

For pores of simple slit or cylindrical geometry, there are two distinct and independent pressures in the confined nanophase, one normal to the wall and one parallel to it (the tangential pressure) [81]. For spherical pores, there are also two such pressures; however, they are related through a first order differential equation [94]. The molecular simulation results show that the normal and tangential pressures are very different in magnitude. Moreover, as seen in figures 14–18, the influences of the main state and system variables on these two pressures are quite different. It is likely that they play different roles in observed phenomena in confined nanophases. It seems quite unlikely that it is possible or profitable to define a single scalar effective pressure for the confined nanophase, as some authors have done.

Acknowledgment

We are grateful to the U.S. National Science Foundation for support of this research under Grant no. CBET-1160151.

Appendix A. Supplementary data

Supplementary data associated with this article can be found, in the online version, at http://dx.doi.org/10.1016/j.jct.2014.01.024.

References

[1] J.C. Maxwell, Nature 17 (1878) 278.
[2] G.M. Wang, E.M. Sevick, E. Mittag, D.J. Searles, D.J. Evans, Phys. Rev. Lett. 89 (2002) 050601.
[3] E.M. Sevick, R. Prabhakar, S.R. Williams, D.J. Searles, Ann. Rev. Phys. Chem. 59 (2008) 603–633.
[4] C.G. Gray, K.E. Gubbins, C.G. Joslin, Theory of Molecular Fluids 2. Applications, Oxford University Press, Oxford, 2011. pp. 733–734, 914–916, Sec. 8.3.
[5] W.A. Steele, Surf. Sci. 36 (1973) 317–352.
[6] W.A. Steele, The Interaction of Gases with Solid Surfaces, Pergamon, Oxford, 1974.
[7] S. Jiang, C. Rhykerd, K.E. Gubbins, Mol. Phys. 79 (1993) 373–391.
[8] M. Miyahara, K.E. Gubbins, J. Chem. Phys. 106 (1997) 2865–2880.
[9] J. Klein, E. Kumacheva, Science 269 (1995) 816–819.
[10] J. Klein, E. Kumacheva, J. Chem. Phys. 108 (1998) 6996–7009; E. Kumacheva, J. Klein, J. Chem. Phys. 108 (1998) 7010–7022.
[11] S.T. Cui, C. McCabe, P.T. Cummings, H.D. Cochran, J. Chem. Phys. 118 (2003) 8941–8944.
[12] R. Radhakrishnan, K.E. Gubbins, M. Śliwinska-Bartkowiak, J. Chem. Phys. 116 (2002) 1147–1155.
[13] M. Kempinski, Y. Long, C. Addington, M. Śliwinska-Bartkowiak, K.E. Gubbins, (2014), in preparation.
[14] D.W. Siderius, L.D. Gelb, J. Chem. Phys. 135 (2011) 084703.
[15] L.D. Gelb, K.E. Gubbins, R. Radhakrishnan, M. Śliwinska-Bartkowiak, Rep. Prog. Phys. 62 (1999) 1573–1659.
[16] C. Alba-Simionesco, B. Coasne, G. Dosseh, G. Dudziak, K.E. Gubbins, R. Radhakrishnan, M. Śliwinska-Bartkowiak, J. Phys. Condens. Matter 18 (2006) R15–R68.
[17] B. Coasne, A. Galarneau, R.J-M. Pellenq, F. Di Renzo, Chem. Soc. Rev. 42 (2013) 4141–4171.
[18] J.A. Duffy, N.J. Wilkinson, H.M. Fretwell, M.A. Alam, R. Evans, J. Phys.: Condens. Matter 7 (1995) L713–L717.
[19] H.M. Fretwell, J.A. Duffy, A.P. Clarke, M.A. Alam, R. Evans, J. Phys.: Condens. Matter 8 (1996) 9613–9619.
[20] D.W. Brown, P.E. Sokol, A.P. Clarke, M.A. Alam, W.J. Nuttall, J. Phys. Condens. Matter 9 (1997) 7317–7325.
[21] C.G.V. Burgess, D.H. Everett, S. Nuttall, Pure Appl. Chem. 61 (1989) 1845–1852.
[22] T.L. Hill, Statistical Mechanics, Principles and Selected Applications, McGraw-Hill, New York, 1956.
[23] B.K. Peterson, K.E. Gubbins, Mol. Phys. 62 (1987) 215–226.
[24] P.B. Balbuena, K.E. Gubbins, Langmuir 9 (1993) 1801–1814.
[25] V. Privman, M.E. Fisher, J. Stat. Phys. 33 (1983) 385–417.
[26] R. Evans, U. Marini, Bettolo Marconi, P. Tarazona, J. Chem. Soc. Faraday Trans. 2 (1986) 1763–1787.
[27] B.K. Peterson, K.E. Gubbins, G.S. Heffelfinger, U. Marini Bettolo Marconi, F. Van Swol, J. Chem. Phys. 88 (1988) 6487–6500.
[28] J.N. Israelachvili, P.M. McGuiggan, A.M. Homola, Science 240 (1988) 189–191.
[29] S. Granick, Science 253 (1991) 1374–1379.
[30] S. Ohnishi, D. Kaneko, J.P. Gong, Y. Osada, A.M. Stewart, V.V. Yaminsky, Langmuir 23 (2007) 7032–7038.
[31] H.W. Hu, G.A. Carson, S. Granick, Phys. Rev. Lett. 66 (1991) 2758–2761.
[32] P.T. Cummings, H. Docherty, C.R. Iacovella, J.K. Singh, AIChE J. 56 (2010) 842–848.
[33] H. Docherty, P.T. Cummings, Soft Matter 6 (2010) 1640–1643.
[34] L. Win, C.R. Iacovella, T.D. Nguyen, H. Docherty, P.T. Cummings, Phys. Rev. B 86 (2012) 214105.
[35] A. Jabbarzadeh, P. Harrowell, R.J. Turner, Macromolecules 36 (2003) 5020–5031.
[36] A. Jabbarzadeh, P. Harrowell, R.J. Turner, Phys. Rev. Lett. 94 (2005) 126103.
[37] B. Coasne, S.K. Jain, L. Naamar, K.E. Gubbins, Phys. Rev. B 76 (2007) 085416.
[38] M. Śliwinska-Bartkowiak, M. Jazdzewska, L. Huang, K.E. Gubbins, Phys. Chem. Chem. Phys. 10 (2008) 4909–4919.
[39] B. Coasne, J. Czwartos, M. Śliwinska-Bartkowiak, K.E. Gubbins, J. Phys. Chem. B 113 (2009) 13874–13881.
[40] M. Śliwinska-Bartkowiak, M. Jazdzewska, K.E. Gubbins, L. Huang, J. Chem. Eng. Data 10 (2010) 4183–4189.
[41] M. Śliwinska-Bartkowiak, F.R. Hung, E.E. Santiso, B. Coasne, G. Dudziak, F.R. Siperstein, K.E. Gubbins, Adsorption 11 (2005) 391–396.
[42] M. Jazdzewska, F.R. Hung, K.E. Gubbins, M. Śliwinska-Bartkowiak, Phys. Chem. Chem. Phys. 7 (2005) 3884–3887.
[43] H. Drozdowski, M. Kempinski, M. Śliwinska-Bartkowiak, M. Jazdzewska, Y. Long, J.C. Palmer, K.E. Gubbins, Phys. Chem. Chem. Phys. 14 (2012) 7145–7153.
[44] L.D. Landau, E.M. Lifshitz, Statistical Physics, third ed., Pergamon Press, London, 1980.
[45] P.M. Chaikin, T.C. Lubensky, Principles of Condensed Matter Physics, Cambridge University Press, Cambridge, 1995. p. 151ff.
[46] R. Radhakrishnan, K.E. Gubbins, Mol. Phys. 96 (1999) 1249–1267.

[47] J.S. van Duijneveldt, D. Frenkel, J. Chem. Phys. 96 (1992) 4655–4668; R.M. Lynden-Bell, J.S. van Duijneveldt, D. Frenkel, Mol. Phys. 80 (1993) 801–814.
[48] N.D. Mermin, Phys. Rev. 176 (1968) 250–254.
[49] R. Radhakrishnan, K.E. Gubbins, M. Śliwinska-Bartkowiak, J. Chem. Phys. 112 (2000) 11048–11057.
[50] H.F. Booth, J.H. Strange, Mol. Phys. 93 (1998) 263–269.
[51] M. Śliwinska-Bartkowiak, G. Dudziak, R. Sikorski, R. Gras, R. Radhakrishnan, K.E. Gubbins, J. Chem. Phys. 114 (2001) 950–962.
[52] S. Takahara, M. Nakano, S. Kittaka, Y. Kuroda, T. Mori, T. Hamano, T. Yamaguchi, J. Phys. Chem. B 103 (1999) 5814–5819.
[53] R. Radhakrishnan, K.E. Gubbins, A. Watanabe, K. Kaneko, J. Chem. Phys. 111 (1999) 9058–9067.
[54] M.W. Maddox, K.E. Gubbins, J. Chem. Phys. 107 (1997) 9659–9667.
[55] K. Morishige, K. Kawano, J. Chem. Phys. 112 (2000) 11023–11029.
[56] M. Śliwinska-Bartkowiak, G. Dudziak, R. Gras, R. Sikorski, R. Radhakrishnan, K.E. Gubbins, Colloids Surf. A 187 (2001) 523–529.
[57] E. Gedat, A. Schreiber, J. Albrecht, T. Emmler, I. Shenderovich, G.H. Findenegg, H.H. Limbach, G. Buntkowsky, J. Phys. Chem. B 106 (2002) 1977–1984.
[58] G. Dosseh, Y. Xia, C. Alba-Simionesco, J. Phys. Chem. B 107 (2003) 6445–6453.
[59] F.R. Hung, G. Dudziak, M. Śliwinska-Bartkowiak, K.E. Gubbins, Mol. Phys. 102 (2004) 223–234.
[60] F.R. Hung, B. Coasne, E.E. Santiso, K.E. Gubbins, F.R. Siperstein, M. Śliwinska-Bartkowiak, J. Chem. Phys. 122 (2005) 144706.
[61] e.g. B. Ratajska-Gadomska, W. Gadomski, J. Chem. Phys. 133 (2010) 234505.
[62] e.g. G. Rother, D. Woywood, M. Schoen, G.H. Findenegg, J. Chem. Phys. 120 (2004) 11864–11873; D. Woywood, S. Schemmel, G. Rother, G.H. Findenegg, M. Schoen, J. Chem. Phys. 122 (2005) 124510.
[63] S. Jiang, K.E. Gubbins, P.B. Balbuena, J. Phys. Chem. 98 (1994) 2403–2411.
[64] E. Kierlik, M.L. Rosinberg, Phys. Rev. A42 (1990) 3382–3387; , Ibid A44 (1991) 5025–5037.
[65] S.L. Sowers, K.E. Gubbins, Langmuir 11 (1995) 4758–4764.
[66] W.T. Góźdź, K.E. Gubbins, A.Z. Panagiotopoulos, Mol. Phys. 84 (1995) 825–834.
[67] P.A. Gordon, E.D. Glandt, J. Chem. Phys. 105 (1996) 4257–4264.
[68] M. Śliwinska-Bartkowiak, S.L. Sowers, K.E. Gubbins, Langmuir 13 (1997) 1182–1188.
[69] M. Śliwinska-Bartkowiak, R. Sikorski, S.L. Sowers, L.D. Gelb, K.E. Gubbins, Fluid Phase Equilib. 136 (1997) 93–109.
[70] L.D. Gelb, K.E. Gubbins, Phys. Rev. E 56 (1997) 3185–3196.
[71] G. Rother, D. Woywood, M. Schoen, G.H. Findenegg, J. Chem. Phys. 120 (2004) 11864–11873.
[72] D. Woywood, S. Schemmel, G. Rother, G.H. Findenegg, M. Schoen, J. Chem. Phys. 122 (2005) 124510.
[73] S. Schemmel, G. Rother, H. Eckerlebe, G.H. Findenegg, J. Chem. Phys. 122 (2005) 244718.
[74] R.R. Meyer, J. Sloan, R.E. Dunin-Borkowski, A.I. Kirkland, M.C. Novotny, S.R. Bailey, J.L. Hutchinson, M.L.H. Greene, Science 289 (2000) 1324–1326.
[75] M. Wilson, J. Chem. Phys. 116 (2002) 3027–3041.
[76] B. Coasne, J. Czwartos, K.E. Gubbins, F.R. Hung, M. Śliwinska-Bartkowiak, Mol. Phys. 102 (2004) 2149–2163.
[77] B. Coasne, J. Czwartos, K.E. Gubbins, F.R. Hung, M. Śliwinska-Bartkowiak, Adsorption 11 (2005) 301–306.
[78] J. Czwartos, B. Coasne, K.E. Gubbins, F.R. Hung, M. Śliwinska-Bartkowiak, Mol. Phys. 103 (2005) 3103–3113.
[79] J. Czwartos, M. Śliwinska-Bartkowiak, B. Coasne, K.E. Gubbins, Pure Appl. Chem. 81 (2009) 1953–1959.
[80] B. Coasne, J. Czwartos, M. Śliwinska-Bartkowiak, K.E. Gubbins, J. Chem. Phys. 133 (2010) 084701.
[81] Y. Long, Pressure tensor of adsorbate in nanoporous materials: molecular simulation studies (Ph.D. Thesis), North Carolina State University, 2012.
[82] K. Kaneko, N. Fukuzaki, K. Kakei, T. Suzuki, S. Ozeki, Langmuir 5 (1989) 960–965.
[83] O. Byl, P. Kondratyuk, J.T. Yates, J. Phys. Chem. B 107 (2003) 4277–4279.
[84] K. Urita, Y. Shiga, T. Fujimori, T. Iiyama, Y. Hattori, H. Kanoh, T. Ohba, H. Tanaka, M. Yudasaka, S. Iijima, I. Moriguchi, F. Okino, M. Endo, K. Kaneko, J.A.C.S. 133 (2011) 10344–10347.
[85] Y. Long, J.C. Palmer, B. Coasne, M. Śliwinska-Bartkowiak, K.E. Gubbins, Phys. Chem. Chem. Phys. 13 (2011) 17163–17170.
[86] Y. Long, J.C. Palmer, B. Coasne, M. Śliwinska-Bartkowiak, G. Jackson, E.A. Müller, K.E. Gubbins, J. Chem. Phys. 139 (2013) 144701.
[87] M. Śliwinska-Bartkowiak, H. Drozdowski, M. Kempinski, M. Jazdzewska, Y. Long, J.C. Palmer, K.E. Gubbins, Phys. Chem. Chem. Phys. 14 (2012) 7145–7153.
[88] e.g. J. Klein, E. Kumacheva, Science 269 (1995) 816–819; J. Klein, E. Kumacheva, J. Chem. Phys. 108 (1998) 6996–7009.
[89] Y. Long, M. Śliwinska-Bartkowiak, H. Drozdowski, M. Kempiński, K.A. Phillips, J.C. Palmer, K.E. Gubbins, Colloids Surf. A: Physicochem. Eng. Aspects 437 (2013) 33–41.
[90] J. Jagiello, J.P. Olivier, Carbon 55 (2013) 70–80.
[91] J. Jagiello, J.P. Olivier, Adsorption 19 (2013) 777–783.
[92] E.A. Müller, K.E. Gubbins, Carbon 36 (1998) 1433–1438.
[93] J. Brennan, T.J. Bandosz, K.T. Thomson, K.E. Gubbins, Colloids Surf. A: Physicochem. Eng. Aspects 187 (2001) 539–568.
[94] Ref. [4], p. 940.

JCT 14-49